CFD VALIDATION USING MULTIPLE INTERFEROMETRIC VIEWS OF THREE DIMENSIONAL SHOCK LAYER FLOWS OVER A BLUNT BODY

R.R. Boyce[*], J.W. Morton[†], A.F.P. Houwing[‡], Ch. Mundt[¶], D.J. Bone[§],
Aerophysics and Laser Diagnostics Research Laboratory
Department of Physics and Theoretical Physics
Australian National University, Canberra ACT 0200 Australia

‡ formerly of Military Aircraft Division, Deutsche Aerospace
Munich, Germany
now at BMW-Rolls Royce Aeroengines
Munich, Germany

§ now at Division of Information Technology
Centre for Spatial Information Systems
Commonwealth Scientific and Industrial Research Organization
Canberra ACT 2601 Australia

Abstract

The validity of the computed three dimensional perfect gas inviscid density field of the shock layer on a blunt body in a hypersonic argon freestream has been investigated. Mach-Zehnder interferometry was used to generate interferograms of such a flowfield produced in the T3 free piston shock tunnel. Using a two dimensional Fourier transform fringe analysis method, two dimensional phase maps (representing line-of-sight integrated density) were produced from the interferograms. Theoretical phase maps, computed from the CFD solution, compare extremely well with the experimental maps for each of seven different viewing angles used to generate interferograms. The multiple angles remove the ambiguity associated with comparing theoretical and experimental integrated quantities. Thus confidence can be placed in the validity of the three dimensional density computations.

Introduction

Increasing importance is being placed on the use of Computational Fluid Dynamics (CFD) codes as engineering tools in the design of new spacecraft. However, before these codes can be applied confidently, it is essential that the numerical methods and physical and chemical models employed by them be thoroughly validated. The final results that represent the combination of the various models and algorithms used in the codes must be extensively checked against experimental data[1].

---

* Research Student, Physics, Student Member AIAA
† Research Student, Physics
‡ Senior Lecturer, Physics, Member AIAA
¶ R & D Research Engineer, Member AIAA
§ Research Scientist

Previous experiments in free piston shock tunnel facilities have produced data on shock shape, surface heat transfer rates and shock layer temperatures, and these have been compared with CFD predictions[2,3,4,5]. In addition, for two-dimensional hypervelocity nitrogen flows over cylinders, it has been possible to make direct comparisons between the interferometrically-measured and CFD-predicted density fields[6,7]. This is because the interferometrically-produced phase data is the result of the integration of the refractive index (and hence the species densities via the Gladstone-Dale relation for a multi-component gas[8]) along the line-of-sight. For a two dimensional flow, the flow parameters are constant along that line-of-sight, and so phase contours in the interferograms correspond directly to refractive index contours in the flowfield. For complex three dimensional flows, however, such direct comparisons are not possible due to the varying flow conditions along the line-of-sight. Instead, the reliability of the code in being able to predict the correct density field needs to be tested indirectly. This can be achieved through using the CFD code to determine theoretical phase maps by performing numerical line-of-sight integration of the density data produced by the code. These phase maps can then be compared with those produced by interferometry experiments. This indirect method has certain short-comings though, since a range of different total and species density distributions can produce identical phase maps, which introduces a certain degree of ambiguity into the CFD validation process.

To overcome this problem, experimental work has been undertaken in order to provide a data base which will eventually be used for the tomographic reconstruction of three-dimensional density distributions in the shock layer around a hyperboloid at nonzero incidence in hypersonic and hypervelocity flows. The data base consists of phase maps for seven different viewing angles of the same flow, and can be used for CFD validation purposes without performing a tomographic reconstruction. This paper presents such validation work, comparing theoretical phase maps generated from the perfect gas three-dimensional coupled Euler/2nd order boundary layer CFD code of

Mundt[9] with the perfect gas part of the experimental data base. The experimental phase maps were produced from interferograms taken of a low stagnation enthalpy hypersonic argon flow generated in the T3 free piston shock tunnel of the Australian National University. The aim is to investigate the validity of the codes density computation by removing the ambiguity of the line-of-sight measurements by using multiple viewing angles. The suitability of the data for tomographic reconstruction can then be discussed.

The Computational Fluid Dynamics method.

The CFD method[9,10] couples the solutions of the Euler and the second-order boundary-layer equations, providing an efficient calculation of the viscous hypersonic flow in regions where boundary-layer theory is valid.

The inviscid flow is solved using a split-matrix algorithm, with Runge-Kutta time stepping, to solve the Euler equations, which are discretized using a third-order accurate upwind biased formula. The equations are then integrated in time using a three step Runge-Kutta procedure. A bow-shock fitting approach is used, with the computational grid extending from the body surface to the shock and therefore time dependent. At the shock, the Rankine-Hugoniot equations are applied, determining the shock velocity (in the transient phase) and shock shape.

The viscous part of the flow is solved using the second-order boundary-layer equations in a locally monoclinic coordinate system. Due to their parabolic behavior in space, these equations are solved with a finite-difference space-marching method. Boundary conditions for to the second-order theory are prescribed at the outer edge of the boundary layer, interpolated from the inviscid profiles delivered from the solution of the Euler equations. This accounts for the effects of entropy layer swallowing.

The coupling procedure, necessary for transferring information between the equation systems, is as follows[10]. An equivalent mass source distribution is calculated from the boundary layer solution, and impressed on the Euler calculation as a boundary condition at the body, filling the region between the body and the displacement thickness with fluid. The resulting equivalent inviscid flow, after convergence, is again coupled to the boundary layer method, after which the calculation is then ended.

Various versions of the code allow the shock layer to be treated as either a perfect gas, equilibrium chemistry flow (by means of vectorized thermodynamic and transport property state surfaces for nitrogen or air[3]) or non-equilibrium chemistry flow[10] (nitrogen or air). A two-dimensional/axisymmetric version is used for 0° angle of attack, while a fully three-dimensional version is used for higher angles of attack. The current work makes use of the 3-d perfect gas code adapted for argon flows.

Producing the flowfield

The shock tunnel facility

The experiments reported here were performed on the Australian National University's T3 free piston shock tunnel[11] (see Figure 1) operated in reflected mode, which produces variable high enthalpy flows as described briefly in the following. A free piston, driven by compressed air, is used to adiabatically compress a gas, known as the driver gas, typically a mixture of helium and argon. This causes a steel diaphragm, separating the driver gas from the test gas, to rupture, which allows a shock wave to propagate along the shock tube through the test gas. The low molecular weight of the driver gas, and the high temperature it attains through compression, enable shock speeds that can be varied from 2 to 7 km/s by an appropriate choice of operating conditions. Upon shock reflection at the end of the shock tube, a stagnant high enthalpy reservoir of test gas is formed (with typical pressure of 20 MPa and stagnation enthalpy that can exceed 20 MJ/kg). The reflected shock wave interacts with the contact surface between the driver and test gases, which either accelerates or attenuates the shock depending on the acoustic impedance change across the contact surface. This interaction causes compression or expansion waves to modify the conditions behind the reflected shock in a nearly isentropic manner. The reservoir feeds into a hypersonic nozzle placed at the end of the shock tube, and the high enthalpy of the reservoir enables hypervelocity flow to be achieved in the test section at the exit of the nozzle. Useful test time decreases with increasing stagnation enthalpy, and is typically of the order of several hundred μs.

The flowfield

The model that was used for the experiment is an axisymmetric hyperboloid defined by the equation

$$(x/491.318 + 1)^2 - (r/86.356)^2 = 1 \qquad (1)$$

where x is the distance in mm along the model axis from its nose, and r is the radial distance in mm. It is 75mm long, with a nose radius of 15.18mm, and is mounted at 15° angle of attack within the Mach cone outside the hypersonic nozzle of T3. The leading part of the model sits 150mm from the nozzle exit during the steady flow period of each shot (for which the tunnel is completely recoiled a distance of 33mm). The nozzle is a 7.5° half-angle conical nozzle (in preference to the contoured nozzle of the previous work, after previous findings[12] in relation to contoured nozzles on shock tunnels) of exit diameter 304.8mm. The model thus sits 1.211m from the nozzle throat, at a physical area

ratio of 183.7, during each shot. Low enthalpy argon was used as the test gas, with the same operating conditions as in previous work[2].

Fig. 1 . a) T3 shock tunnel with interferometer, b) Mach Zehnder interferometer

the test section flow consists of a reasonably uniform core surrounded by the nozzle wall boundary layer. The 'uniform' core displays some structure which is due in part to the shot
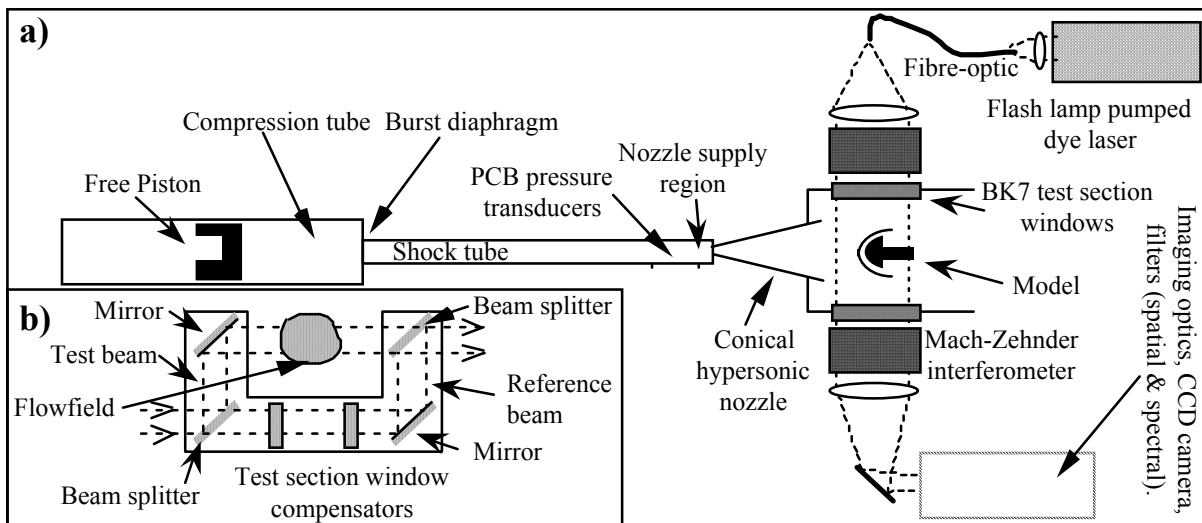
Determination of the freestream conditions

The conditions of the flow in the test section were selected by appropriate choices for the partial pressures of argon and helium in the driver gas, the diaphragm rupture pressure, and the shock tube fill pressure. The pressures and transit times of the primary shock wave were measured with two PCB 113A23 piezoelectric transducers placed 830mm and 80mm from the end of the shock tube. The second transducer also monitored the nozzle supply pressure. Table 1 gives the chosen operating conditions for the tunnel, and the measured primary shock velocity. The freestream conditions in the test section at the location of the model were determined as follows. Firstly, the nozzle supply conditions were calculated by well established shock tube theory from the measured primary shock speed and nozzle reservoir pressure. Secondly, the effective nozzle area ratio was determined using measured freestream pitot pressures and an understanding of the nozzle boundary layer behavior. Thirdly, with a knowledge of the effective nozzle area ratio, the freestream conditions were calculated by theoretical models that describe inviscid nonequilibrium expansion flow.

For CFD validation purposes, the freestream conditions (including gradients and flow quality) must be known accurately[1]. Firstly, a separate set of experiments at the same operating conditions were run in which a pitot pressure rake (one PCB 113A21 and three PCB 112A21 transducers) was used over several shots to build up pitot pressure profiles across the nozzle exit and across the freestream flow at the location of the model. These profiles, measured at the same post-shock reflection delay as the interferometry, are shown in Figure 2. As the figure shows,

to shot variations of the tunnel. However, the overall shape of the structure appears at both locations along the nozzle, and probably represents nonuniformities propagating along the flow. For the purposes of determining the freestream conditions, the flow has been assumed to be uniform across the flow, with pitot pressure levels of 211.6 ± 11 kPa at the nozzle exit and 169.8 ± 7 kPa at the location of the front of the model. The uncertainties quoted are the standard deviations of the pitot pressure measurements, and represent the spread of pitot pressure assuming it does vary across the nozzle.

Using the initial conditions in the shock tube, and the measured shock speed and nozzle supply pressure, the computer program ESTC[13] was used to calculate the conditions behind the reflected shock and then the nozzle supply conditions via an isentropic expansion/compression. Due to the drainage of the test gas through the nozzle, and the wave processes occurring in the nozzle supply region, the nozzle supply pressure exhibits the behavior shown in Figure 3, where drainage is followed by overtailoring. Since the nozzle supply is thus changing with time, knowledge of the time (called here the nozzle transit time, t_{NT}) taken for waves to relay a change in nozzle supply pressure to the test section is needed. This time is then subtracted from the time at which the experiment was performed to give the time and conditions in the nozzle supply region appropriate to the experiment. To calculate this time, the conditions throughout the nozzle, as well as the wave processes within the nozzle supply region (which affect the pressure measured by the transducer situated some 45mm from the start of the convergence towards the nozzle throat) must be known. The effect of these processes will be small however, since pressure gradients in the nozzle supply region will be

3

much less than in the nozzle itself, and so the nozzle transit time can be represented as $t_{NT} = \int dx/(v+a)$, where x is the distance from the end of the nozzle supply region, v is the flow velocity and a is the speed of sound. The integration is performed along the nozzle centerline from the start of the converging section to the location of the model. These parameters are determined by performing a one dimensional inviscid nozzle calculation with the computer program NENZF[14], and using the true nozzle contour to give the area ratio variation with distance along the nozzle. The nozzle transit time was found to be extremely slowly varying with changing area ratio, as long as the nozzle length was constant. This is due to the compensating effect of a decreasing area ratio for given location causing an increased sound speed but a decreased velocity. An approximation to this nozzle transit time is given by the time difference between the incident shock passing the nozzle supply pressure transducer, propagating through the nozzle, and reaching the model (or pitot pressure rake). This time difference for the present work was $t_S = 440\mu s$. Two sets of nozzle supply conditions, calculated with ESTC at times that straddled the approximation given by t_S, were used to calculate limiting values for the nozzle transit time of $440\mu s$ and $463\mu s$, from which limiting nozzle supply conditions were determined and then averaged. From these average conditions, a final nozzle transit time was calculated as $453\mu s$, and then final nozzle supply conditions were determined. These were a nozzle supply pressure of 17.4 ± 0.4 MPa, a nozzle supply temperature of 6590 ± 120 K, and a nozzle supply ('stagnation') enthalpy of 3.43 ± 0.06 MJ/kg. The variation of nozzle supply pressure with fluctuations in the time at which the interferometry was performed is about ± 0.2 MPa. Variations from shot to shot are of approximately the same magnitude, while variations over a conservative error in the nozzle transit time of ± 50 μs are also ± 0.2 MPa.
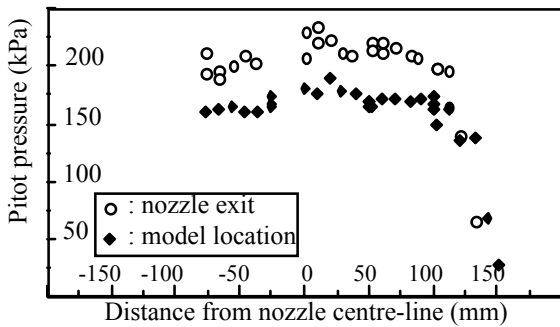

Fig. 2 . Pitot pressure profiles across the nozzle flow.

Table 1 T3 Operating Conditions	
Reservoir pressure	4.51 MPa air
Driver gas initial pressure	78.9 kPa Ar, 26.7 kPa He
Shock tube initial pressure	106.4 kPa Ar
Primary shock velocity	1840 ms^{-1}

With knowledge of the nozzle supply conditions, the nozzle flow can be calculated using the two-dimensional inviscid nonequilibrium chemistry program SURF[15]. At first the true nozzle contour is used, and then the area ratios that give the measured pitot pressures are used to determine an effective nozzle angle that accounts for the nozzle boundary layer. SURF is then run again using this angle and the calculated conditions at the location of the model used as the freestream conditions for the CFD code.
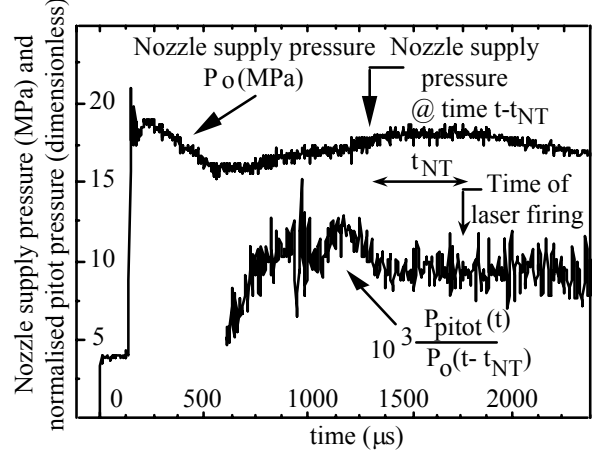

Fig. 3. Nozzle supply pressure and freestream pitot pressure.

To confirm the present use of this method of accounting for the nozzle wall boundary layer, an alternative method was also used as follows. Edenfield[16,17] determined from measurements from various hypersonic windtunnels that the displacement thickness δ^* is given by

$$\delta^*/x = 0.42 \, (Re_{ref})^{-0.2775} \qquad (2)$$

where x the distance from the nozzle throat, and Re_{ref} the reference Reynolds number:

$$Re_{ref} = \rho_{ref}.v_\infty.x/\mu_{ref} \, . \qquad (3)$$

Here v_∞ is the freestream velocity at x , while ρ_{ref} and μ_{ref} are the density and viscosity evaluated at the freestream pressure p_∞ and Eckert's reference enthalpy[18] :

$$h_{ref} = 0.5(h_W + h_\infty) + 0.22(h_{ad} - h_\infty) \, . \qquad (4)$$

Here h_W is the wall enthalpy, while h_{ad} is the adiabatic enthalpy :

$$h_{ad} = h_\infty + r(h_{stg} - h_\infty) \, . \qquad (5)$$

For a turbulent boundary layer, r (the recovery factor) = $(Pr)^{1/3}$, where Pr is the Prandtl number.

This correlation was applied as follows : SURF was used to calculate the conditions at the exit of the nozzle as a function of nozzle angle. The correlation was used to

4

determine the displacement thickness there for each angle. A geometrical displacement thickness can be defined as the true nozzle exit radius (152.4mm) minus the effective radius for each angle. As the angle is decreased from its true value, the Edenfield displacement thickness also decreases, whereas the geometrical displacement thickness sharply rises. The angle for which the two values for displacement thickness agree is the nozzle angle that is consistent with the Edenfield boundary layer correlation as applied to the present physical nozzle.

By running SURF for this effective angle of 6.60° (nozzle half-angle), the pitot pressures at the nozzle exit and model location were determined to be 217.7 kPa and 171.4 kPa respectively, which agree with the experimental values. Hence the experimental pitot pressure results used here to account for the nozzle wall boundary layer are in agreement with results from other facilities. The effective area ratio at the model tip is thus $A/A^* = 145$.

narrowband spectral filtering, the wavelength λ was 589.1nm (FWHM = 0.6nm). Spatial filtering was also used in the collection optics, with both forms of filtering serving the purpose of eliminating the luminosity associated with flow impurities being excited by the high temperatures in the shock layer. With fringes focused at the plane of the model, the interferogram was imaged onto a CCD camera such that one dimension of the camera, parallel to the freestream, caught approximately 30mm of the model and 25mm of the freestream. This was sufficient to resolve 18 pixels between the model and the bow shock at the stagnation streamline.

Two interferograms were taken for each shot - a 'no flow' reference interferogram just prior to the shot, and a test interferogram during the shot. Each digitized interferogram was stored on a PC for later processing and conversion into phase shift maps.

Table 2 Nozzle Supply Conditions, Freestream Conditions & Gradients				
Nozzle Supply Conditions		Freestream :	Conditions	Gradients
Pressure P_O	17.4 ± 0.4 MPa	Pressure P_∞	680.8 ± 8% Pa	-5%
Temperature T_O	6590 ± 120 K	Temperature T_∞	113.6 ± 1% K	-2%
Enthalpy h_O	3.43 ± 0.06 MJ/kg	Velocity v_∞	2596 ± 2% ms^{-1}	+0.02%
Density ρ_O	12.7 ± 0.3 kg/m^3	Density ρ_∞	0.02880 ± 7% kg/m^3	-3%
Nozzle transit time	453 μs	Mach number M_∞	13.06 ± 2%	+1%

The freestream values and gradients at the location of the model are given, along with the nozzle supply values, in Table 2. The key values that affect this work are Mach number = 13.06 and density = 0.0288 kg/m^3. They change by +1% and -3% respectively in the direction of streamlines, over the region analyzed in this work, due to the conicity of the flow. The maximum freestream angular deflection from the nozzle centerline over the region presented is 0.7°. Thus the effects of axial and radial flow gradients in the current work due to the use of a conical nozzle can be ignored. The uncertainties quoted for the freestream parameters were calculated by applying the variations in nozzle reservoir conditions and measured freestream pitot pressure to the nozzle flow calculation. This gives the possible variation of Mach number and density across the freestream, which will affect the shock layer density field and hence the experimental phase maps. The small uncertainties quoted for the temperature and velocity represent the variation of those quantities when tied by perfect gas laws to the varying pressure and density.

Control of the experiment

The PC also controlled the firing of the laser. This was done after a preset delay had elapsed after arrival of a trigger signal from the primary shock passing the nozzle supply region pressure transducer. The delay was chosen to be 1750μs (and actually varied up to 50μs each way from shot to shot) to coincide with the plateau of the nozzle supply pressure, shown on Figure 3. The figure also shows the ratio

$$10^3 P_{pitot}(t)/P_0 \, (t - t_{NT}) \qquad (6)$$

for one of the pitot survey shots, at 50mm off centerline at the location of the model. Steady flow exists where this ratio is a constant, and commences approximately 1400 μs after the primary shock arrival in the nozzle supply region. Thus the current work utilized steady flow, but was done not too long after steady flow onset to avoid the problem of driver gas contamination.

Interferometry

To probe the density distribution in the shock layer, a Carl Zeiss Mach-Zehnder interferometer was used to produce finite-fringe interferograms of the flowfield and freestream, as shown in Figure 1. The light source used was a home made grating tuned flash lamp pumped dye laser (FLPDL) operating with the laser dye Rhodamine 6G. After

To compare the predictions of the CFD code with the experimental data, theoretical phase maps are computed by applying the interferometer equation[8] along lines-of-sight through the flowfield. This equation relates the total phase shift ϕ of light, with wavelength λ, propagating along each line-of-sight, to the refractive index **n** of the fluid at each point :

5

$$\phi = 2\pi/\lambda \int (\mathbf{n} - 1) \, ds \quad . \tag{7}$$

The integration is along the line-of-sight, with ds being the distance increment. The refractive index is determined using the Gladstone-Dale equation

$$\mathbf{n} - 1 = \Sigma_i \, \mathbf{K}_i \rho_i \tag{8}$$

where $\mathbf{K}_i$ are the Gladstone-Dale coefficients, and ρ_i the densities, for each species i in the gas. For the ideal gas argon flow under consideration, equation (7) becomes

$$\phi = 2\pi \mathbf{K}/\lambda \int \rho \, ds \quad . \tag{9}$$

For the present work, λ = 589.1 nm, for which K = 1.58×10^{-4} m^3/kg (interpolated from the data presented by Leonard[19]). A Cartesian coordinate system $\mathbf{u},\mathbf{v},\mathbf{w}$ is set up such that $\mathbf{u}$ lies along the direction of the freestream flow and $\mathbf{v}$ lies along the line-of-sight across the flowfield. Integration is performed along each $\mathbf{v}$ ray (which are spaced by the pixel dimensions in the experimental data), with the integrated phase shift forming a map in the $\mathbf{u},\mathbf{w}$ plane. The limits of integration are the same for each ray and lie outside the shock layer. At the end of the calculation the phase shift ϕ_∞ that would exist in the absence of the model is subtracted from ϕ to yield the phase shift due to the blunt body flow only.

An interpolation from the curvilinear body-centered coordinate system of the CFD code to the Cartesian system of the phase integration is performed to give the density at each point along each ray. In order to avoid time consuming grid searches to achieve this, the analytical shape of the model is used to determine in which curvilinear grid cell each point on the line-of-sight lies. The interpolation is then performed in computational (grid indice) space rather than physical space. This has the added advantage that the interpolated density varies smoothly along each ray.

As was discussed previously, a total of seven different viewing angles (in 15° increments from the position of the model, at attack, being side-on to the optical axis) were employed in order to remove the ambiguity associated with the measurement of an integrated flow parameter. This was achieved by rotating between shots the central sting holding the model.

Image processing

The raw interferograms contain phase information not only for the flowfield being investigated, but also from sources such as the spatial profile of the laser, imperfections in the optics, background luminosity (admittedly minimized here by the filtering employed) and random noise. To extract the flowfield phase information from each interferogram, the semi-automated two-dimensional Fourier transform fringe analysis software FrAnSys[20] was used.

The 2-D Fourier transform technique makes use of the separation in the Fourier transform plane of many of the contributions to the interferograms intensity distribution, due to the heterodyning process (the production of finite fringes by tilting an interferometer component). Writing the distribution of phase across the interferogram $\phi'(\mathbf{r})$ as $\phi'(\mathbf{r}) = \phi(\mathbf{r}) + \phi_1(\mathbf{r})$, where $\phi(\mathbf{r})$ is the phase due to the flowfield and $\phi_1(\mathbf{r})$ is the phase due to optics imperfections, we define the quantity $q(\mathbf{r}) = \exp(i \, \phi'(\mathbf{r}))$. We can then write the intensity distribution, expanded as a Fourier series to include the second harmonic (to account for any non-linearity in the recording medium response) across the finite fringe interferogram as

$$\begin{aligned} i(\mathbf{r}) = \, &1/2 \, m(\mathbf{r}) \, q(\mathbf{r}) \exp(2\pi i \, \mathbf{v_0} \cdot \mathbf{r}) + \\ &1/2 \, m(\mathbf{r}) \, q^*(\mathbf{r}) \exp(-2\pi i \, \mathbf{v_0} \cdot \mathbf{r}) + \\ &1/2 \, h(\mathbf{r}) \, (q(\mathbf{r}))^2 \exp(4\pi i \, \mathbf{v_0} \cdot \mathbf{r}) + \\ &1/2 \, h(\mathbf{r}) \, (q^*(\mathbf{r}))^2 \exp(-4\pi i \, \mathbf{v_0} \cdot \mathbf{r}) + \\ &b(\mathbf{r}) + n(\mathbf{r}) \end{aligned} \tag{10}$$

where $\mathbf{r}$ is the position vector, $\mathbf{v_0}$ the vector heterodyning frequency, $i(\mathbf{r})$ the intensity, $m(\mathbf{r})$ the amplitude of the fringes (modulated by the laser beam profile), $b(\mathbf{r})$ is the background illumination, $n(\mathbf{r})$ is the random noise, and $h(\mathbf{r})$ is the low-frequency modulation of the second harmonic (related to $m(\mathbf{r})$, $b(\mathbf{r})$ and the response function of the recording medium). '*' denotes the complex conjugate.

The intensity distribution in the Fourier transform plane is then

$$\begin{aligned} I(\mathbf{v}) = \, &1/2 \, M \otimes Q(\mathbf{v} - \mathbf{v_0}) + \\ &1/2 \, M \otimes Q^*(-\mathbf{v} - \mathbf{v_0}) + \\ &1/2 \, H \otimes Q \otimes Q(\mathbf{v} - 2\mathbf{v_0}) + \\ &1/2 \, H \otimes Q^* \otimes Q^*(-\mathbf{v} - 2\mathbf{v_0}) + \\ &B(\mathbf{v}) + N(\mathbf{v}) \end{aligned} \tag{11}$$

where $\otimes$ is the convolution operator, and capital letters are the 2-D Fourier transforms of the lower case intensity components.

From equation (11) we can see that the phase information from the flow is separated from the other components in the transform plane, being located in regions centered at frequencies $\pm \mathbf{v_0}$. These regions may be small or large, depending on the range of the fringe shifts and the angle the shifted fringes lie at. Thus by filtering out all other components in the transform plane, the component located at frequency $+ \mathbf{v_0}$, labeled

$$G(\mathbf{v}) = 1/2 \, M \otimes Q(\mathbf{v} - \mathbf{v_0}) \tag{12}$$

can be selected. Upon retransforming, this yields

$$g(\mathbf{r}) = 1/2 \, m(\mathbf{r}) \exp(i \, [\, 2\pi \, \mathbf{v_0} \cdot \mathbf{r} + \phi'(\mathbf{r}) \,]) \, . \tag{13}$$

Some theoretical restrictions apply to the magnification and fringe spacing of the interferogram. The choice of heterodyning frequency does not affect the size of G, but simply translates its position relative to the other components. ν_0 needs to be chosen large enough to separate G from the other components completely. On the other hand, the finite area of data processed means that if ν_0 is too large then aliasing of the second harmonic back onto the fundamental can occur. A final consideration in the production of the interferograms is the requirement that the camera pixels represent at least two samples per fringe[20]. The interferograms of the current work meet these restrictions.

To retrieve the phase information, Equation (13) can be manipulated to give

$$2\pi \, \mathbf{v_0} \cdot \mathbf{r} + \phi'(\mathbf{r}) = \tan^{-1}[\text{Im}(g(\mathbf{r}))/\text{Re}(g(\mathbf{r}))] . \quad (14)$$

However, this quantity is determined as modulo 2π of the true phase, wrapped into the interval $-\pi$ to π. The true phase is recovered using an unwrapping technique[21]. To remove the heterodyning and optics contributions we subtract a similar result gained from a no-flow interferogram, which does not contain $\phi(\mathbf{r})$. Thus the phase is recovered :

$$\phi(\mathbf{r}) = [2\pi \, \mathbf{v_0} \cdot \mathbf{r} + \phi'(\mathbf{r})]_{flow} - [2\pi \, \mathbf{v_0} \cdot \mathbf{r} + \phi_1(\mathbf{r})]_{no\text{-}flow} . \quad (15)$$

This is only a first approximation, however : the subtracting of the two results relies on aligning the two interferograms, and this introduces a slight rotational misalignment uncertainty manifested as an additional linear background component of the phase. There is also the possibility of slight changes occurring to the heterodyning between the recording of each interferogram. For a more accurate result, a region in the first approximation to the phase distribution that is known to be undisturbed by the flow is chosen. The method of least-squares is used to fit a plane to this region, and this plane is then subtracted from the entire distribution, removing the linear background and accounting for possible changes to the heterodyning (the plane is fitted to a region that is effectively a no-flow region). In the current work, the region upstream of the shock was chosen, and assumed to have negligible variation of phase shift, since (as previously stated) the flow gradients are small and the variation of path length through the test core is also negligible across the small size of the region of interest. The result is the phase shift due to the shock layer only. However, after performing this subtraction, a one-dimensional (perpendicular to the freestream) modulation of the phase remained, suggestive of inhomogeneities across the nozzle propagating downstream. This was dealt with for cross-sections of the images between the model and the bow shock as follows : the region outside the shock formed by those cross-sections, plus one or two cross-sections just upstream of the shock, was averaged in the streamwise direction to give an average cross-section of the modulation. This was then subtracted from each cross-section in the entire image, leaving the freestream for cross-sections between the shock and model free of all modulation except high frequency noise.

In the 2-D Fourier transform, the image is assumed to be one period of a continuous infinite cycle. To avoid the problem of discontinuities at the boundary of the image (and at the edge of the model) causing streaking of information across the Fourier plane, FrAnSys enlarges the image by adding a strip of zeros outside each border, and iteratively extends the fringes into the new region and into the model so that they vary continuously across each boundary. This is done by transforming the extended data, retransforming a small region around the heterodyning frequency and the origin, merging the original data back in, and iterating, with gradually increasing filter size, until a smooth fringe extension is achieved.

Results

Using the methods described above, experimental phase maps were produced from which the various non-flow phase contributions (except for some random noise) have been removed. In addition, phase maps, with freestream phase subtracted, were computed from the inviscid solution by the CFD method for the present conditions. The boundary layer has negligible effect on the structure of the inviscid shock layer at these conditions, and so phase maps for an uncoupled (inviscid only) solution are presented.

Figure 4a is a digitized interferogram for a shot with viewing angle θ (the angle between the optical axis of the interferometer and the normal of the plane defined by the central axes of both the nozzle and model) equal to 60°. The dimensions of each unextended image are 320 x 100 pixels, with each pixel representing 0.143 ± 0.001 mm horizontally and 0.203 ± 0.001 mm vertically. The direction of the freestream flow is along the vertical (**u**) direction, and the stagnation point lies at the middle of the image. The fringe shift at the bow shock, as well as various chips (due to diaphragm fragment hits) on the test section windows, can be clearly seen. The interferogram shown does not include the fringe extension. Figure 4b is the 2-D Fourier transform of the extended form of the interferogram in Figure 4a. Rising well above the noise are peaks at frequencies $\nu = 0$ (low frequency background information, for example the spatial modulation of the FLPDL), $\nu = \pm \nu_o$ (the flow information clustered around the heterodyning frequency) and higher order harmonics, most probably due to non-linearities in the gain of the CCD camera. Clearly, the flow information is separated from the other contributions to the interferogram by the heterodyning. Figures 5 and 6 show "20-color" images for both experimental and theoretical phase maps for the two extremes of the seven viewing angles used ($\theta = 0°$ and $\theta = 90°$). The comparison between the theoretical and experimental phase maps is extremely good, given the noise present in the experimental maps, for both cases. Some noise can be seen in the freestream region

of Figure 5a. In general, for each viewing angle, fluctuations across the experimental phase maps are less than 5% of the maximum phase shift in each case. Another feature of Figures 5 and 6 is the good agreement between the experimental and theoretical shock shapes.

It is appropriate at this point to describe the uncertainties in the comparisons due to positioning errors : uncertainties in the calibration of the scale of the experimental interferograms have led to slight scale differences between the theoretical and experimental images; the uncertainty in the determination of the stagnation point of the model from the interferograms has led to slight translational uncertainties between the images; and uncertainty in the original viewing angle ($\pm$ 2°) has led to slight shape differences between experimental and theoretical body outlines.
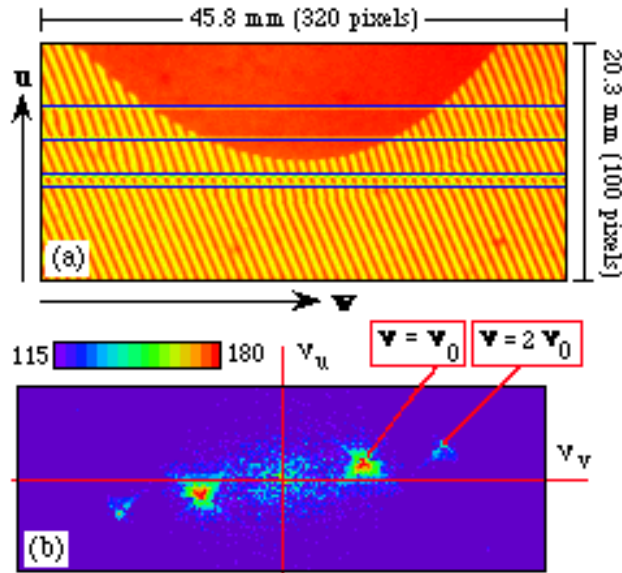
Fig. 4 (a) Interferogram for $\theta = 60°$ (not extended). Horizontal lines represent slices (from top of frame) 75, 61, 46 and 41. (b) Contour plot of 2-D Fourier transform of fig. 4a. (after extension).

Overall, there is possibly up to a 3-4 pixel uncertainty in any direction when comparing the experimental and theoretical phase shifts at any given point. The stagnation streamline shock standoff comparison shows at most a 1-2 pixel discrepancy (~5-10% of the standoff distance) in each case.

The flow geometry chosen in the experiments is expected to produce a flow which is symmetric on reflection through the plane defined by the nozzle and model axes. Because of the non-zero angle of incidence of the model to the flow, however, the flow will be asymmetric on reflection through any other plane. In the nose region, the flow is expected to have near-axial symmetry because of the spherical shape of the body surface there. Deviation from axial symmetry is expected to increase with distance downstream from the nose. Figure 7(a-c) show line contour plots for three view angles. In all three contour plots, the departure from axial symmetry is quite noticeable and, with the exception of the contour for $\phi = 3.5$ in Figure 7a, the agreement between theory and experiment is good. Figure 8 (a-c) show the phase shift profiles for a number of horizontal slices through the phase maps for the extreme viewing angles $\theta = 0°$ and $\theta = 90°$. For $\theta = 0°$, the departure from axial symmetry is very pronounced for slice 75, for which the theory predicts the phase shift on the windward surface to be about 44% larger than that on the leeward surface. The experimental result shows a slightly larger departure from symmetry, with the phase shift on the windward surface being measured to be approximately 68% larger than that on the leeward surface.

Three possible explanations for the discrepancy between theory and experiment are considered here: the CFD code is in error and is underpredicting the density or the shock standoff distance in this region of the flow; in the experiment, the freestream flow is nonuniform with a higher density and lower Mach number flow incident on the
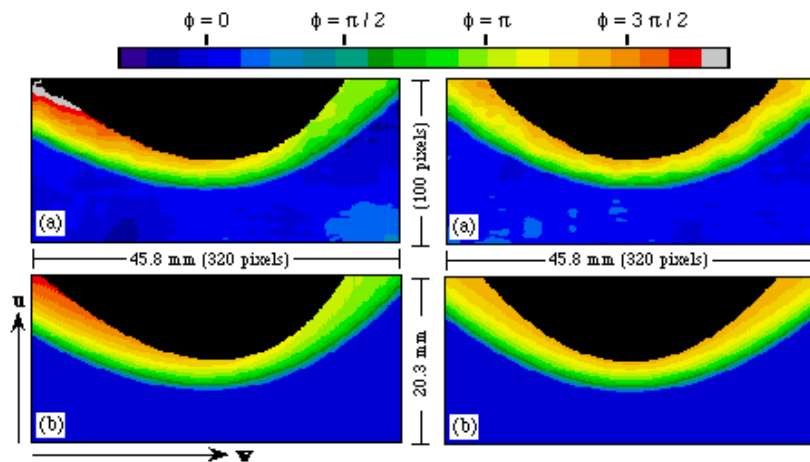

Fig. 5. Phase maps for $\theta = 0°$ (a) experiment, (b) theory.

Fig. 6. Phase maps for $\theta = 90°$ (a) experiment, (b) theory.

windward surface; or pixel misalignment is causing slightly different slices to be compared. At the hypersonic Mach numbers generated by the T3 shock tunnel, shock standoff distance for near-normal shock waves will not be sensitively dependent on variations in Mach number. However, regions of lower Mach number will not have experienced the same degree of expansion as regions of higher Mach number. Hence, in lower Mach number regions, the gas density will be higher, giving a larger phase shift in the shocked region. It is noteworthy that in Figure 8a, two theoretical profiles are given for each slice. One profile is for the lower limit of the freestream density $(\rho_\infty - \Delta\rho_\infty)$, while the other is for the upper limit of the freestream density $(\rho_\infty + \Delta\rho_\infty)$. Comparing the two theoretical profiles with the experimental profile indicates that a variation of $2\Delta\rho_\infty$ in density between the flow incident upon the windward and leeward surfaces would be sufficient to account for the discrepancy. Figure 8b is similar to Figure 8a except that the mean value for the freestream density is used for the theoretical calculation and 2 adjacent theoretical slices are given for each experimental slice. The comparison here shows the same discrepancy between theory and experiment for slice 75 and thus suggests that pixel misalignment is not the cause for the discrepancy. For slices 41 and 46, the agreement between theory and experiment is reasonable, though small discrepancies do exist.
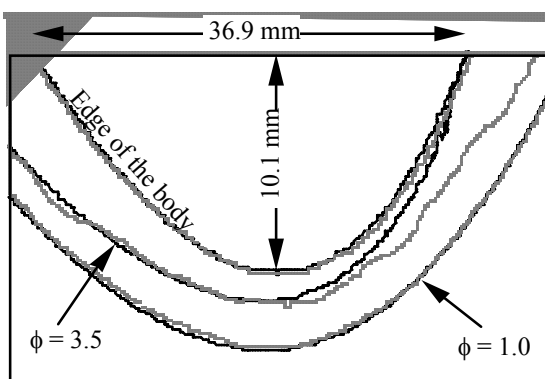

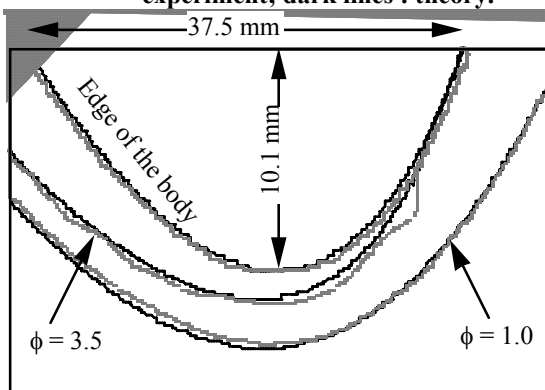**Fig.. 7a. Phase shift contours for θ = 30˚. Faint lines : experiment; dark lines : theory.**

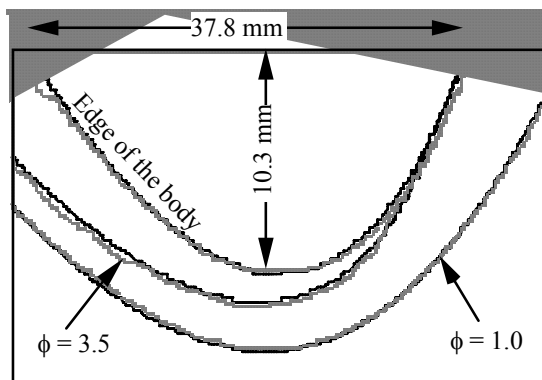**Fig 7b. Phase shift contours for θ = 15˚. Faint lines : experiment; dark lines : theory.**

Fig. 7c. Phase shift contours for θ = 0˚. Faint lines : experiment; dark lines : theory.

The significant departure of the flow from axial symmetry can be demonstrated through Figure 9, which shows a surface plot of the phase shift for the θ = 0° line of sight. The increase in phase shift as one moves away from the shock vertex is due mainly to an increase in the optical pathlength through the shock layer, rather than an increase in density. For meaningful comparison of phase shifts, one needs to compare regions for which optical pathlengths are similar. This is expected to be the case when comparing a point on the windward surface with a point on the leeward surface for the same value of **u** (i.e. on the same slice). Hence, we can conclude with reasonable confidence that, for slice 75, the average density near the windward surface is about 68% higher than that near the leeward surface.

In addition to examining phase shifts, an examination of the experimental and theoretical shock shapes is an important test on the validity of the CFD code. Figure 10 shows a comparison between experimental and theoretical shock shapes for slices 46 and 61. For each slice the experimental shock shape was obtained from the seven line of sight projections as follows. For a particular slice and line of sight, the projection of the shock shape gives the distance for two shock tangents from the axis of rotation. Both tangents are directed along the line of sight. The distance of a shock tangent from the axis of rotation is measured along a line which is perpendicular to both the tangent and rotation axis. This information gives the equation of the tangent in the plane of the slice, but not the exact location of a point (hereafter called the shock point) on the shock front. To obtain an estimate of the position of a shock point for a particular θ, we use an approximate technique that involves the shock tangents obtained for θ − Δθ, θ and θ + Δθ. The shock point is estimated to lie on the shock tangent for θ at a position which is halfway between the point of intersection of the tangents for θ − Δθ and θ and the point of intersection of the tangents for θ + Δθ and θ. Because of the reflection-type symmetry of the flow and the large number of viewing angles adopted, the error in locating the shock point with this method is expected to be

small. Once the position of the shock points have been estimated, the complete shock front for a given slice is determined by fitting a smooth curve through all the shock points. Note that, because of the reflection-type symmetry, each view direction, with the exception of $\theta = 90°$, produces four shock tangents rather than two. Hence, for the seven different viewing angles, we obtain a total of 26 shock points.
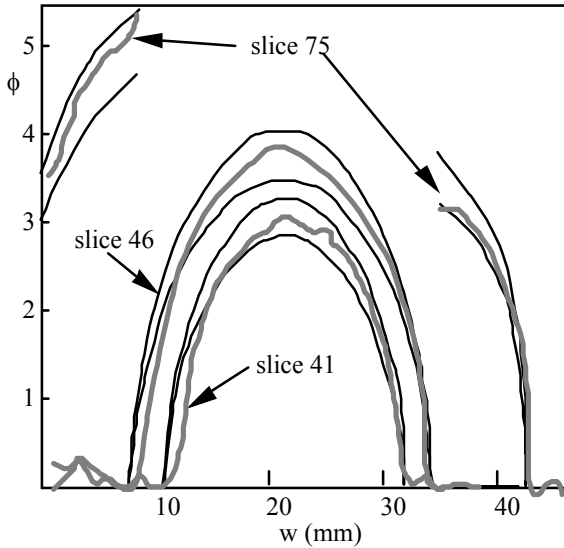

Fig. 8a. Phase shift profiles along rows (slices) with constant u for $\theta = 0°$. Faint lines : experiment; dark lines : theory. For each slice, two theoretical profiles are given, corresponding to the error limits of the free stream density.
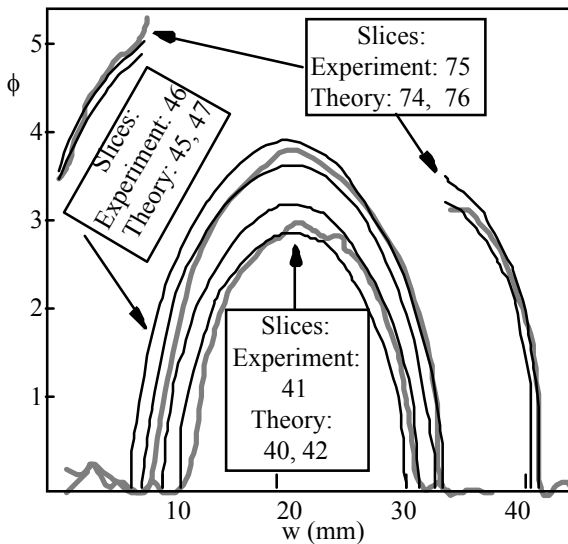
Fig. 8b. Phase shift profiles for $\theta = 0°$. Faint lines : experiment; dark lines : theory.

From Figure 10, we see that the agreement between theory and experiment is good. Both the experimental and theoretical shock shapes are deformed ellipses, which are symmetrical with respect to reflection through the long axis but asymmetric with respect to reflection through the short axis. The shock shapes shown in this figure allow us to

determine the optical pathlengths for each of the different viewing directions. In particular, this information allows us to justify the assumption made earlier when discussing the phase shifts in the surface plot of Figure 9. Note that the experimental shock shapes were determined from the analyzed phase, which suffers from a significant reduction in resolution at the shock because of the high frequency filtering in the Fourier transform plane. A more accurate comparison is possible by using the original interferograms. The "flat regions" in the experimental shock shape are an artifact of the reconstruction method used and are not expected to exist in the actual flows.
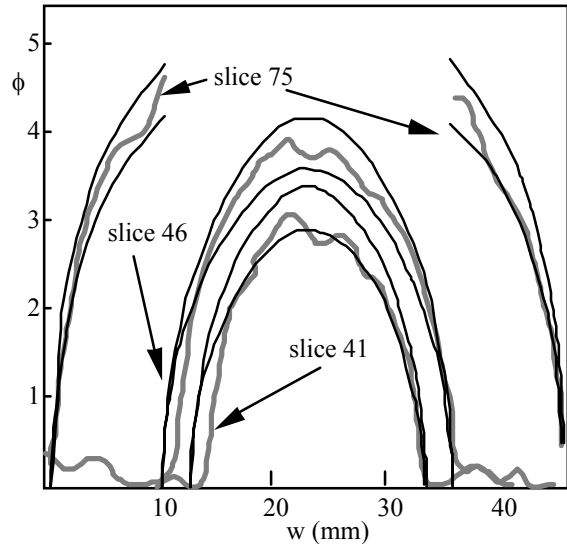

Fig. 8c. Phase shift profiles along rows (slices) with constant u for $\theta = 90°$. Faint lines : experiment; dark lines : theory. For each slice, two theoretical profiles are given, corresponding to the error limits of the free stream density.
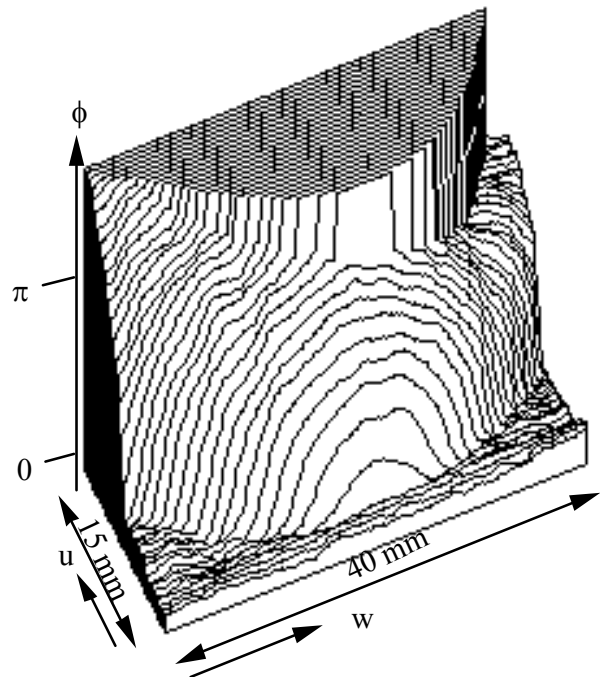

Fig. 9. Experimental phase shift surface plot for $\theta = 0°$.

10

Conclusions

The current study has provided a valuable comparison between experimentally measured and theoretically calculated flow fields. By obtaining interferometric projections for a large number of lines of sight, it has been possible to study a non-axially-symmetric shock-layer flow field. The theoretically predicted phase maps and shock shapes compare well with the experimental results. Discrepancies that do exist between theory and experiment are explainable in terms of small nonuniformities in the flowfield. This work has completed an important preliminary step required before the implementation of tomographic reconstruction methods. Furthermore the results obtained in the current study will provide a valuable data base for the tomographic reconstruction work. In an analogous fashion, the experiments with a perfect gas flow are an important initial step in the code validation process for the more general case of nonequilibrium real gas flows.
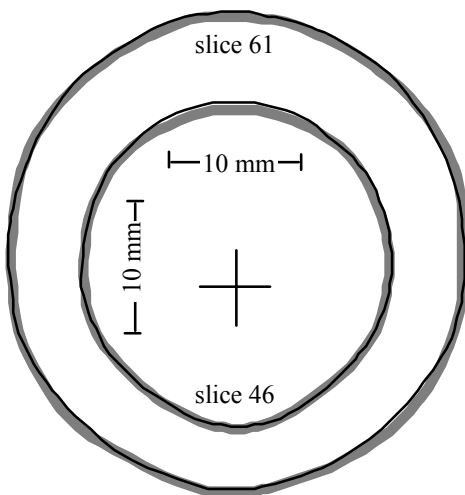

Fig. 10. Shock shapes for slices 46 and 61. Faint lines : experiment; dark lines : theory. The cross marks the axis of rotation for the different views.

Acknowledgments

References

1. Chapman, G.T., "An overview of hypersonic aerothermodynamics", *Comm. App. Num. Meth.*, Vol. 4, pp. 319-325, 1988.
2. Boyce, R.R., Mundt, Ch., "Aeronautical CFD Studies of Reentry Flows", *Proc. Int. Aerospace Congress*, Vol. 3, pp. 23-31, 1991.
3. Boyce, R.R., Mundt, Ch., "Computational Fluid Dynamics Code Validation using a Free Piston Hypervelocity Shock Tunnel", *Shock Waves*, Vol. 2, pp. 1127-1132, Springer-Verlag, 1991.
4. Boyce, R.R., Pulford, D.R.N., Houwing, A.F.P., Mundt, Ch., Sandeman, R.J., "Comparisons of Nonequilibrium Chemistry CFD calculations with broadband CARS measurements of local temperatures in hypervelocity nitrogen blunt body flows", *Proc. 19th Int. Symp. Shock Waves*, Marseille, 1993.
5. Sutton, D.J., Houwing, A.F.P., Palma, P.C., Boyce, R.R., Sandeman, R.J., "The application of Laser Induced Predissociation Fluorescence to the Measurement of Vibrational Temperatures in a Shock Layer Flow", *AIAA Paper 93- 3071*, 1993.
6. Hornung, H.G., "Nonequilibrium dissociating flow over spheres and circular cylinders", *J. Fluid Mech.*, Vol. 53, pp. 149-176, 1972.
7. Park, C., Yoon, S., "A Fully-Coupled Implicit Method for Thermo-Chemical Nonequilibrium Air at Sub-Orbital Flight Speeds", *AIAA Paper,* 89-1974, 1989.
8. Merzkirch, W., "Flow Visualization", Academic Press, 1987.
9. Monnoyer, F., Mundt, Ch., Pfitzner, M., "Calculation of the hypersonic viscous flow past reentry vehicles with an Euler-boundary layer coupling method", *AIAA Paper 90-0417*, 1990.
10. Mundt, Ch., "Calculation of hypersonic, viscous, non-equilibrium flows around reentry bodies using a coupled boundary layer/Euler method", *AIAA Paper 92-2856*, 1992.
11. Stalker, R.J., "Development of a Hypervelocity Wind Tunnel", *Aero. J. Roy. Aero. Soc.*, Vol. 76, p. 374, 1972.
12. Mudford, N., Personal communication, 1991.
13. McIntosh, M.K., "Computer program for the numerical calculation of frozen and equilibrium conditions in shock tunnels", *ANU Internal Report,* 1968.
14. Lordi, J.A., Mates, R.E., Moselle, J.R., "Computer program for the numerical solution of nonequilibrium expansions of reacting gas mixtures", *CAL Report AD-1689-A-6,* 1965.
15. Rein, M., "SURF : A Program for Calculating Inviscid Supersonic Reacting Flows in Nozzles", *GALCIT FM 89-1*, 1989.
16. Edenfield, E.E., "Contoured Nozzle Design and Evaluation for Hotshot Wind Tunnels", *AIAA Paper 68-369,* 1968.
17. Edenfield, E.E., "Design of a High Reynolds Number Mach Number 8 Contoured Nozzle for the Hypervelocity Wind Tunnel (F)", *AEDC-TR-72-48,* 1972.
18. Eckert, E.R.G., "Engineering Relations for Friction and Heat Transfer to Surfaces in High Velocity Flow", *J. Aeronautical Sciences,* Vol. 22, No. 8, pp. 585-587, 1955.

19. Leonard, P.J., "Refractive Indices, Verdet Constants and Polarizabilities of the Inert Gases", *Atomic and Nuclear Data Tables*, Vol. 14, pp. 21-37, 1974.
20. Bone, D.J., "A Users Guide to FrAnSys- a Fringe Analysis System from Australian National University", *ANU Internal Report,* 1991.
21. Bone, D.J., "Fourier fringe analysis : the 2-D phase unwrapping problem", *Appl. Opt.*, Vol. 30, No. 25, pp. 3627-3632, 1991.